Bidirectional Chopper With Single-Cell Auxiliary Full-Bridge Converter for Onboard Battery Energy Storage System

Ghiffari Aby Malik Nasution, *Student Member, IEEE*, Masaki Matsumoto, and Makoto Hagiwara, *Senior Member, IEEE*

***Abstract*—This article focuses on a bidirectionalchopper with an auxiliary converter for onboard battery energy storage systems. The auxiliary converter is made of single-phase full-bridge cells connected in cascade, which can function as an active power filter. This setup aims to reduce both the switching-ripple current of the inductor (i.e., inductance) and its associated volume. However, using multiple cells could lead to an eventual rise of the converter loss and cost. To mitigate these issues, a single-cell auxiliary converter is proposed. Subsequently, the inductor switching-ripple current, inductor volume, and power loss in the chopper are evaluated. Theoretical analysis shows that the use of single-cell auxiliary converter in the chopper can reduce the maximum switching-ripple current to 4/9 of that the conventional bidirectional chopper under the same switching frequency. Further, the validity of the theoretical analysis and the steady- and transient-state performances of the proposed chopper are experimentally verified using a 2 kW downscaled model. Finally, the efficacy of the proposed chopper is verified through a comparison with respect to the inductor volume, power loss, and efficiency, with the conventional bidirectional chopper, the three-level flying capacitor converter, and the bidirectional chopper with auxiliary converter using three cells.**

***Index Terms*—Battery energy storage systems (BESSs), nonisolated dc–dc converters.**

I. Introduction

RECENTLY, the issues of using catenary lines to power electric railway have been highlighted, which include disrupted daily life caused by the installation of overhead cables, reliance on electricity grids to inject and absorb power during peak demands, and energy losses due to the regenerative braking system [1], [2], [3]. In order to mitigate these issues, battery energy storage system (BESS) has been considered due to its ability to charge and discharge the regenerative-braking energy, limit the catenary voltage drop during acceleration, shave peak power, and allow catenary-free operation [4], [5], [6]. Meanwhile, a bidirectional chopper is conventionally used for voltage conversion between the power source and the battery, where the typical voltages range from 600 V to 3 kV [7], [8], [9], [10], [11].

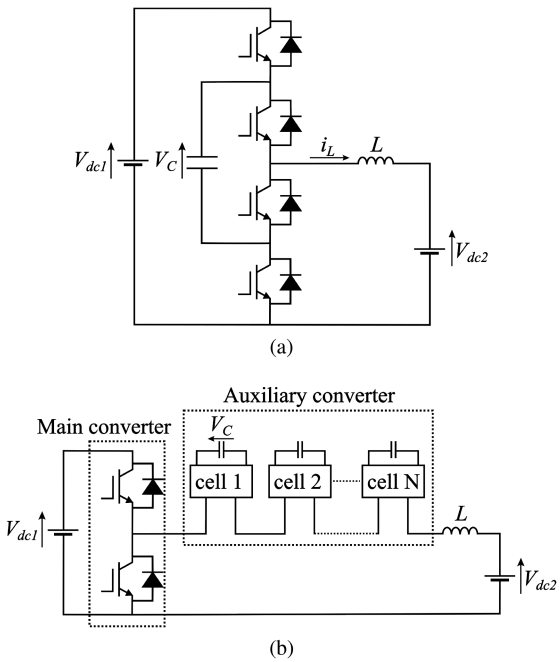

Fig. 1. Conventional multilevel DC–DC converters. (a) TLFC DC–DC converter [14], [15], [16]. (b) Bidirectional chopper with auxiliary converter [30], [31], [32], [33], [34], [35].

When the BESS is installed, the reduction of mass and volume of the inductor in the conventional bidirectional chopper (CBC) becomes necessary, since it is placed in a moving train car. One way to achieve this is by lowering the inductance value through increasing the switching frequency of the power devices. However, when the switching losses of the devices are considered, an upper limit for the switching frequency exists. For example, under a catenary voltage of 1.5 kV, the typical switching frequency for 3.3-kV Si-IGBT modules is 600 Hz, while that of 3.3-kV SiC-MOSFET is 2 kHz [12], [13].

Several attempts to reduce the inductor volume using multilevel converter topologies have been previously done. Fig. 1(a) shows the circuit configuration of a dc–dc converter based on three-level flying capacitor (TLFC) that can produce three voltage levels of 0, V_C, and V_{dc1} [14], [15], [16]. If the

Manuscript received 13 November 2023; revised 7 March 2024; accepted 13 April 2024. Date of publication 24 April 2024; date of current version 20 June 2024. Recommended for publication by Associate Editor F. J. Azcondo. *(Corresponding author: Ghiffari Aby Malik Nasution.)*

The authors are with the Department of Electrical and Electronic Engineering, Tokyo Institute of Technology, Meguro-ku 152-8550, Japan (e-mail: nasution.g.aa@m.titech.ac.jp; matsumoto.m.be@m.titech.ac.jp; hagiwara@ee.e.titech.ac.jp).

Color versions of one or more figures in this article are available at https://doi.org/10.1109/TPEL.2024.3392923.

Digital Object Identifier 10.1109/TPEL.2024.3392923

dc-capacitor voltage, V_C, is set to be half of the dc-source voltage, $V_{\rm dc1}$ (i.e., $V_C = V_{\rm dc1}/2$), and no phase shift is considered in its operation, the TLFC can work as a bidirectional chopper with the voltage of $V_{\rm dc1}/2$ at the high-voltage side and $V_{\rm dc2}$ at the low-voltage side, or that with $V_{\rm dc1}/2$ at the high-voltage side and $V_{\rm dc2} - V_{\rm dc1}/2$ at the low-voltage side. Consequently, the maximum peak-to-peak current can be reduced to 1/2 of that the CBC under the same switching frequency [17]. Because of this merit, numerous studies with focus on its control and applications in power systems have been conducted [18], [19], [20]. However, the TLFC suffers from complex controls, where the control of the inductor current and that of the dc-capacitor voltage are strongly coupled [21], [22]. Similar problems occur when flying-capacitor converters with more than three levels are applied.

A topology called the resonant switched-capacitor converter (RSCC) with its magnetic-less structure, where flying capacitor is utilized to transfer energy to the output has been proposed [23], [24], [25]. But, the RSCC typically suffers from limitations on the current and voltage rating of the capacitor, increased number of active switches, and high switching loss under hard switching [26], [27]. The last problem can be solved through the application of soft switching, or zero-current switching, by connecting a small inductor to the capacitor in series to form a resonant circuit [28]. However, there is a limited range of voltage in which the soft switching can be achieved [29].

Fig. 1(b) shows the circuit configuration of the bidirectional chopper with the auxiliary converter (BCAC) [30], [31], [32], [33], [34], [35]. BCAC utilizes the CBC as its main converter and adds an auxiliary converter based on multiple cascaded full-bridge converter cells. The auxiliary converter is able to reduce the switching-ripple current by working as an active power filter that cancels the ac voltage produced by the main converter. To do this, the switching frequencies of the main converter, f_{SM}, needs to be equal or less than that of the auxiliary converter, f_{SA} (i.e., $f_{SM} \leq f_{SA}$). If f_{SA} is increased, the ripple frequency will also increase. Further, to make sure that the auxiliary converter can work as an active power filter under all conditions when $V_{\rm dc1} \geq V_{\rm dc2}$, the relationship $NV_C \geq V_{\rm dc1}$ should hold, where N is the number of cells in the auxiliary converter, $V_{\rm dc1}$ and $V_{\rm dc2}$ are the dc-voltage sources, and V_C is the dc-capacitor voltage connected to the full-bridge cell. It should be noted that only reactive power is processed by the auxiliary converter in the BCAC ideally, with no active power. Thus, the BCAC is a full power converter, and not a partial power dc–dc converter that processes a percentage of the converter total power [36].

In [30] and [31], the switching-ripple current can be reduced to 1/60 of that the CBC by setting $N = 3$, $f_{SA} = 4f_{SM}$, and $V_C \leq V_{\rm dc1}/3$. The auxiliary converter can equivalently work as a solid-state dc circuit breaker, which is not included in the CBC and TLFC. Further, the decouple of controls between the inductor current and the dc-capacitor can be achieved because both the main and auxiliary converters can work as independent voltage sources. In [32] and [33], interleaved topologies utilizing BCAC have been proposed. The mass and volume reductions can be achieved by setting $N = 3$, $M = 3$, $f_{SA} = 4f_{SM}$, and $V_C = V_{\rm dc1}/3$, where M is the number of subconverters in the interleaved topology. In Hagiwara and Ahmad's [34] work, the high-frequency performance of the BCAC has been described. In Ahmad and Hagiwara's [35] work, a noninverting BCAC that is able to operate in buck, buck-boost, and boost modes has been proposed. The proposed chopper has significantly lower mass and volume compared to its conventional counterpart. However, it suffers from increased power loss and potentially the cost, due to the installations of multiple cells in the auxiliary converter.

The aim of this article is to solve the above-mentioned problems by applying the following three conditions to the BCAC.

1) The number of the cells is one ($N = 1$).
2) $f_{SA} = f_{SM}$.
3) $V_C = V_{\rm dc1}/2$.

Although the reduction of power loss and cost can be achieved by applying the above-mentioned conditions to the BCAC, the switching-ripple current may increase instead because of the decrease in the frequency of the ripple component (due to the second condition) and the limitation of the auxiliary converter function as an active power filter (due to the third condition). Thus, a detailed theoretical analysis of the switching-ripple current will be required. In other words, the performance of the proposed chopper will be evaluated based on: 1) switching-ripple current, 2) inductor volume reduction, and 3) power loss produced by the chopper. Some parts of the theoretical analysis has been carried out in Nasution et al.'s [37] work. However, the detailed derivation process under the wide operating voltage range is not disclosed. To the best of our knowledge this article, no study has focused on the BCAC under the above-mentioned conditions.

The rest of this article is organized as follows. Section II presents the proposed chopper topology and operating principles. Section III discusses the control methods applied to the main and auxiliary converters. Section IV details the theoretical analysis on the switching-ripple current of the proposed chopper. Section V gives the comparison results of the inductor volume and power loss between the proposed chopper, CBC, TLFC, and BCAC with three cells. Section VI shows the steady- and transient-states experimental results of the proposed chopper. Finally, Section VII concludes this article.

II. Circuit Configuration and Operating Principles

A. Circuit Configuration

Fig. 2 shows the circuit configuration of the proposed bidirectional chopper with a single-cell auxiliary converter (BCSAC), where $V_{\rm dc1}$ is the high-voltage-side voltage, $V_{\rm dc2}$ is the low-voltage-side voltage, v_L is the inductor voltage, and i_L is the inductor current. S_1 and S_2 denote the upper and lower power devices of the main converter, respectively, and v_M is the low-voltage-side voltage of the main converter. In the auxiliary converter, S_3 and S_4 denote the upper and lower power devices of one leg that is connected to the main converter, respectively, while S_5 and S_6 denote those of another leg that is connected to the inductor. v_A is the auxiliary converter voltage and v_C is the dc-capacitor voltage, where the relationship $V_C = V_{\rm dc1}/2$

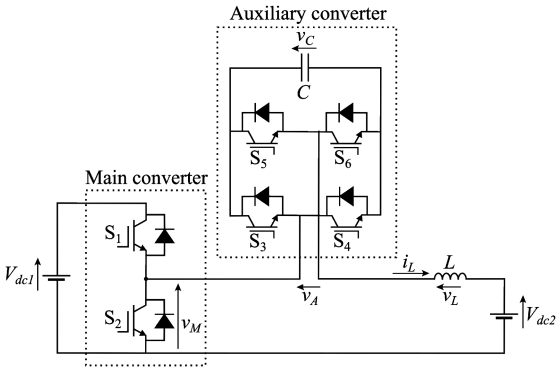

Fig. 2. Proposed topology of the BCSAC.

holds regarding the dc component as mentioned in the previous section.

The triangular carrier applied to the main converter, tri_M, is the same as that applied to the auxiliary converter, tri_A. Consequently, the frequency of tri_M, f_{SM}, and that of tri_A, f_{SA}, are the same (i.e., $f_{SM} = f_{SA}$). Further, the equivalent switching frequency of v_A is $2f_{SA}$, due to the unipolar PWM applied to the auxiliary converter.

It should be noted that sawtooth carrier(s) can be applied to the legs of the auxiliary converter instead of applying the triangular carrier. The choice of the carrier waveform may affect the performance of the converter in terms of the switching-ripple components. However, the analysis of the switching-ripple components when other carriers are applied is beyond the scope of this article and it is left for future work.

B. Operating Principles

When the deadtime is zero, v_M in the BCSAC is given by

$$v_M = \begin{cases} V_{\text{dc1}} & (\text{S}_1 : \text{ON}, \text{S}_2 : \text{OFF}) \\ 0 & (\text{S}_1 : \text{OFF}, \text{S}_2 : \text{ON}) \end{cases} \tag{1}$$

where v_M has both the dc component, $(v_M)_{\text{dc}}$, and the ac component, $(v_M)_{\text{ac}}$. If the duty ratio of S_1 is assumed to be d_M, $(v_M)_{\text{dc}}$ is given by

$$(v_M)_{\text{dc}} = d_M V_{\text{dc1}}. \tag{2}$$

From (1) and (2), $(v_M)_{\text{ac}}$ is given by

$$(v_M)_{\text{ac}} = \begin{cases} (1-d_M)V_{\text{dc1}} & (\text{S}_1 : \text{ON}, \text{S}_2 : \text{OFF}) \\ -d_M V_{\text{dc1}} & (\text{S}_1 : \text{OFF}, \text{S}_2 : \text{ON}). \end{cases} \tag{3}$$

To enable the auxiliary converter to function as an active power filter, its ac output has to be equal to that of the main converter [i.e., $(v_A)_{\text{ac}} = (v_M)_{\text{ac}}$]. Based on (3), the maximum value of $(v_M)_{\text{ac}}$ is V_{dc1}, while its minimum value is $-V_{\text{dc1}}$. On the other hand, V_C must satisfy the following condition in the operation:

$$V_C \geq |(v_A)_{\text{ac}}|. \tag{4}$$

From (3) and (4), $V_C \geq V_{\text{dc1}}$ must hold to enable the auxiliary converter to function as an active power filter under all conditions where $V_{\text{dc1}} \geq V_{\text{dc2}}$. However, to further reduce the switching loss, V_C in this article is set to

$$V_C = 0.5V_{\text{dc1}}. \tag{5}$$

Consequently, if the auxiliary converter intends to produce the ac voltage $(v_M)_{\text{ac}}$ given by (3), a dc component may occur as a result of overmodulation in the converter. Considering that v_A is an ac component and i_L is a dc component, the auxiliary converter only processes the reactive power.

Based on (4) and (5), normalization should be applied to $(v_A)_{\text{ac}}$ to limit its value to

$$-0.5V_{\text{dc1}} \leq (v_A)_{\text{ac}} \leq 0.5V_{\text{dc1}}. \tag{6}$$

Under the normalization, the value of $(v_M)_{\text{ac}}$ relative to the d_M given by (3) is regulated to eliminate the overmodulation problem. For example, the relationship $(v_M)_{\text{ac}} \geq 0.5V_{\text{dc1}}$ always holds under $0 \leq d_M < 0.5$, when S_1 is ON and S_2 is OFF. In this case, $(v_A)_{\text{ac}}$ is fixed to $0.5V_{\text{dc1}}$ under the said condition. Further, the average value of $(v_A)_{\text{ac}}$ in one switching period T should be zero

$$\int^{T} (v_A)_{\text{ac}} dt = 0. \tag{7}$$

Considering (6) and (7), $(v_A)_{\text{ac}}$ when $0 \leq d_M < 0.5$ is given by

$$(v_A)_{\text{ac}} = \begin{cases} 0.5V_{\text{dc1}} & (\text{S}_1 : \text{ON}, \text{S}_2 : \text{OFF}) \\ -dV_{\text{dc1}} + \frac{{d_M}^2 - 0.5d_M}{d_M - 1} & (\text{S}_1 : \text{OFF}, \text{S}_2 : \text{ON}). \end{cases} \tag{8}$$

Meanwhile, the relationship $(v_M)_{\text{ac}} \leq -0.5V_{\text{dc1}}$ always holds under $0.5 \leq d_M \leq 1$, when S_1 is OFF and S_2 is ON. In this case, $(v_A)_{\text{ac}}$ is fixed to $-0.5V_{\text{dc1}}$ under the said condition. Similarly, $(v_A)_{\text{ac}}$ when $0.5 \leq d_M \leq 1$ is given by

$$(v_A)_{\text{ac}} = \begin{cases} (1-d_M)V_{\text{dc1}} + \\ \frac{{d_M}^2 - 1.5d_M + 0.5}{d_M} V_{\text{dc1}} & (\text{S}_1 : \text{ON}, \text{S}_2 : \text{OFF}) \\ -0.5V_{\text{dc1}} & (\text{S}_1 : \text{OFF}, \text{S}_2 : \text{ON}). \end{cases} \tag{9}$$

Considering (3), (8), and (9), the relationship $(v_M)_{\text{ac}} = (v_A)_{\text{ac}}$ holds when $d_M = 0.5$. In this situation, the auxiliary converter nullifies the frequency component of f_{SM} in $(v_M)_{\text{ac}}$, resulting in the absence of the frequency component of f_{SM} in the inductor current. On the contrary, the relationship $(v_M)_{\text{ac}} = (v_A)_{\text{ac}}$ does not hold when $d_M \neq 0.5$. In this situation, the frequency component of f_{SM} persists in the inductor current.

III. Control Method

The control method of the BCSAC circuit can be separated into:

- inductor current control;
- dc-capacitor control.

The control method closely resembles the one introduced in Ahmad and Hagiwara's [35] work, but differing primarily in the current control. While Ahmad and Hagiwara's [35] work achieves current control through the main converter, this article employs the auxiliary converter to undertake that function. Since the switching frequency of the auxiliary converter is two times that of the main converter, as has been described in Section II, a more precised current controllability can be achieved.

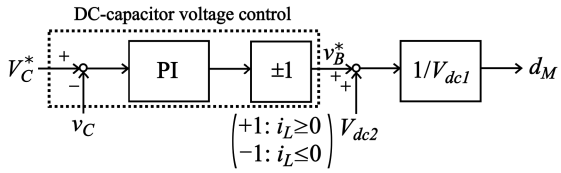

Fig. 3. Control block diagram of the main converter.

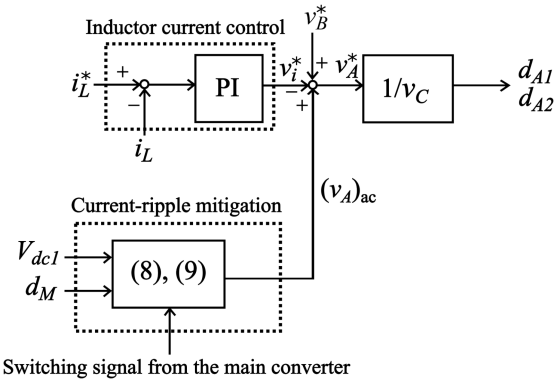

Fig. 4. Control block diagram of the auxiliary converter.

A. Main Converter Control

Fig. 3 shows the control block diagram of the main converter. The objective of the main converter control is to regulate the dc-capacitor voltage using the traditional PI control. To be more precise, the voltage reference v_B^* is generated to make the difference between the dc-capacitor voltage, v_C, and its reference value, V_C^*, become zero. It should be noted that the polarity of v_B^* should be changed based on that of the inductor current (i.e., v_B^* under $V_C^* > v_C$ is positive when i_L is positive, while v_B^* under $V_C^* > v_C$ is negative when i_L is negative). Subsequently, $V_{\rm dc2}$ is added to v_B^* as a feedforward control, followed by the normalization by $V_{\rm dc1}$. As a result, the duty ratio of S_1, d_M, is produced. d_M has a maximum value of unity and a minimum value of zero.

To explain the principle of the dc-capacitor voltage control, a positive dc-inductor current of $i_L = I_L(>0)$ is assumed to flow in the circuit. The dc power at the high-voltage side of the main converter is given from (2) and Fig. 3 as

$$(v_M)_{\rm dc} I_L = d_M V_{\rm dc1} I_L = (v_B + V_{\rm dc2}) I_L \tag{10}$$

where v_B is the actual voltage used for the dc-capacitor voltage control, and the relationship $v_B = v_B^*$ is assumed to hold.

When $v_C = V_C^*$, $(v_M)_{\rm dc} I_L$ and the dc power at the low-voltage side (i.e., $V_{\rm dc2} I_L$) are the same because $v_B = 0$. Hence, no power flows in the auxiliary converter. When $v_C < V_C^*$, a positive v_B^* occurs, and a positive power is formed between v_B and I_L, which is superimposed on $(v_M)_{\rm dc} I_L$. This means that the relationship $(v_M)_{\rm dc} I_L > V_{\rm dc2} I_L$ holds in the circuit. Simultaneously, the auxiliary converter receives this power by producing v_B^*, as will be shown in Fig. 4. As a result, a positive power $V_{\rm dc2} I_L$ flows into the auxiliary converter and v_C increases. In other words, all the additional power superimposed on the main converter flows to the auxiliary converter. It should be noted that the voltage component v_B^* produced by the main and auxiliary converters cancel each other out so that it does not affect the current control. Thus, the decouple of controls between the dc-capacitor voltage and the inductor current can be achieved.

B. Auxiliary Converter Control

Fig. 4 shows the control block diagram of the auxiliary converter. The objectives of the auxiliary converter control are as follows.

1) Inductor current control.
2) Ripple-current mitigation.

The inductor current control utilizes the traditional PI controller to generate the voltage command v_i^*, based on the difference between its actual value, i_L, and its reference value, i_L^*. Subsequently, $(v_A)_{\rm ac}$, given by (8) and (9), and the voltage reference v_B^* are added to v_i^* as a feedforward control. It produces the voltage reference of the auxiliary converter, v_A^*, which is then normalized by v_C. As a result, the duty ratio of S_3, d_{A1}, and that of S_5, d_{A2}, are produced. It should be noted that d_{A1} and d_{A2}, initially ranging from a maximum value of $+1$ to a minimum value of -1 in Fig. 4, will be further normalized to have a maximum value of $+1$ and a minimum value of zero. Finally, these values are compared with $\rm tri_A$, which has a maximum value of $+1$ and a minimum value of zero.

The difference between v_B^* and v_i^* is described in the following. When there is no power loss in the converter, the relationship $v_B^* = 0$ holds under the steady state. Meanwhile, the relationship $v_i^* \neq 0$ holds under the same condition due to the existence of a dc voltage in v_A, which originates from the pulse-width modulation. To achieve the current control, the dc voltage should be canceled by v_i^*. In other word, the dc component of v_i^* is necessary to realize the one-period average value of v_A to be zero, as shown by (7). The value of v_i^* will also affect the value of the ripple current, as will be mentioned later.

IV. Theoretical Analysis of Switching-Ripple Current

In the theoretical analysis of the switching-ripple current, the following assumptions are used.

1) Steady state is considered.
2) The deadtime of the main and auxiliary converters are zero.
3) v_B^* used for the dc-capacitor voltage control is zero.
4) The relationship $V_C = V_{\rm dc1}/2$ holds where the ac component in the dc-capacitor voltage is assumed to be zero.

The validity of the second assumption holds when the deadtime period is sufficiently shorter than the switching period. The validity of the third assumption holds under the steady state with no power loss, as described in Section III.

Under the second assumption ($v_B^* = 0$), d_M is expressed as

$$d_M = \frac{V_{\rm dc2}}{V_{\rm dc1}}. \tag{11}$$

It should be noted that d_M, d_{A1}, and d_{A2} can be compared with $\rm tri_M$ because the relationship $\rm tri_M = tri_A$ holds, as mentioned in

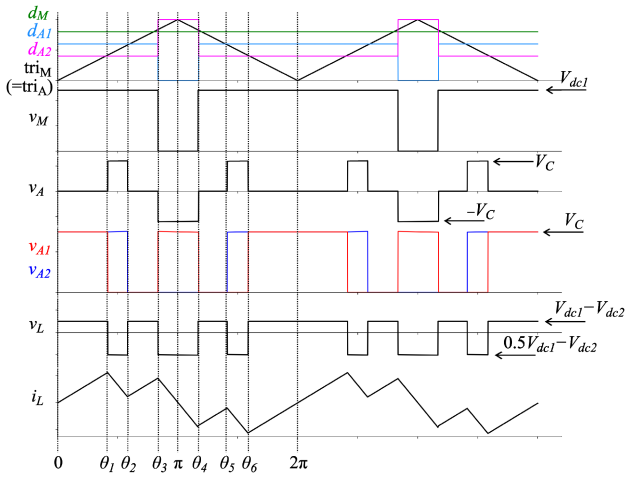

Fig. 5. Ideal voltage and current waveforms when $d_M = 0.75$.

Section II. Further, the following analysis focuses on the case when $0.5 \le d_M \le 1$.

Fig. 5 shows the example of the ideal voltage and current waveforms when $d_M = 0.75$. Let the phases where d_M and tri_M intersect each other be θ_3 and θ_4, respectively. They are given from Fig. 5 as follows:

$$\theta_3 = \pi d_M \tag{12}$$

$$\theta_4 = 2\pi - \pi d_M \tag{13}$$

where the relationship $\theta_3 \le \theta_4$ always holds. Meanwhile, v_M is given by

$$v_M = \begin{cases} V_{\text{dc1}} & (0 \le \theta \le \theta_3, \theta_4 \le \theta \le 2\pi) \\ 0 & (\theta_3 < \theta < \theta_4). \end{cases} \tag{14}$$

From (9) and Fig. 4, the duty ratios d_{A1} and d_{A2} ($-1 \le d_{A1} \le 1$, $-1 \le d_{A2} \le 1$) are given by

$$d_{A1} = \begin{cases} -\frac{2v_i^*}{V_{\text{dc1}}} - 1 + \\ \frac{1}{d_M} & (0 \le \theta \le \theta_3, \theta_4 \le \theta \le 2\pi) \\ -\frac{2v_i^*}{V_{\text{dc1}}} - 1 & (\theta_3 < \theta < \theta_4) \end{cases} \tag{15}$$

$$d_{A2} = \begin{cases} \frac{2v_i^*}{V_{\text{dc1}}} + 1 - \frac{1}{d_M} & (0 \le \theta \le \theta_3, \theta_4 \le \theta \le 2\pi) \\ \frac{2v_i^*}{V_{\text{dc1}}} + 1 & (\theta_3 < \theta < \theta_4) \end{cases} \tag{16}$$

where $d_{A2} = -d_{A1}$ holds because unipolar PWM is applied. Subsequently, d_{A1} and d_{A2} are normalized to the ranges of $0 \le d_{A1} \le 1$ and $0 \le d_{A2} \le 1$

$$d_{A1} = \begin{cases} -\frac{v_i^*}{V_{\text{dc1}}} + \frac{0.5}{d_M} & (0 \le \theta \le \theta_3, \theta_4 \le \theta \le 2\pi) \\ 0 & (\theta_3 < \theta < \theta_4) \end{cases} \tag{17}$$

$$d_{A2} = \begin{cases} \frac{v_i^*}{V_{\text{dc1}}} + 1 - \frac{0.5}{d_M} & (0 \le \theta \le \theta_3, \theta_4 \le \theta \le 2\pi) \\ 1 & (\theta_3 < \theta < \theta_4). \end{cases} \tag{18}$$

In the following, these points are assumed.

- d_{A1} intersects tri_M at θ_2 and θ_5.
- d_{A2} intersects tri_M at θ_1 and θ_6.

Fig. 5 shows that the relationships $\theta_1 \le \theta_3$, $\theta_2 \le \theta_3$, $\theta_4 \le \theta_6$, and $\theta_5 \le \theta_6$ are held. Based on (17) and Fig. 5, θ_2 and θ_5 are given as

$$\theta_2 = \pi \left(-\frac{v_i^*}{V_{\text{dc1}}} + \frac{0.5}{d_M} \right) \tag{19}$$

$$\theta_5 = 2\pi - \pi \left(-\frac{v_i^*}{V_{\text{dc1}}} + \frac{0.5}{d_M} \right). \tag{20}$$

Meanwhile, based on (18) and Fig. 5, θ_1 and θ_6 are given as

$$\theta_1 = \pi \left(\frac{v_i^*}{V_{\text{dc1}}} + 1 - \frac{0.5}{d_M} \right) \tag{21}$$

$$\theta_6 = 2\pi - \pi \left(\frac{v_i^*}{V_{\text{dc1}}} + 1 - \frac{0.5}{d_M} \right). \tag{22}$$

Considering θ_1 through θ_6, v_A is given by

$$v_A = \begin{cases} 0 & (0 \le \theta \le \theta_1) \\ V_C & (\theta_1 < \theta \le \theta_2) \\ 0 & (\theta_2 < \theta \le \theta_3) \\ -V_C & (\theta_3 < \theta \le \theta_4) \\ 0 & (\theta_4 < \theta \le \theta_5) \\ V_C & (\theta_5 < \theta \le \theta_6) \\ 0 & (\theta_6 < \theta \le 2\pi). \end{cases} \tag{23}$$

The power supplied into the auxiliary converter is given by $v_A i_L$. When i_L is a dc quantity, v_i^* will be adjusted so that v_A under the steady state contains only the ac component. Hence, the following relationship holds:

$$\int_0^{2\pi} v_A \, d\theta = V_C(\theta_2 + \theta_3 + \theta_6 - \theta_1 - \theta_4 - \theta_5) = 0$$

$$\therefore \theta_2 + \theta_3 + \theta_6 - \theta_1 - \theta_4 - \theta_5 = 0. \tag{24}$$

Substituting (12), (13), (19), (20), (21), and (22) into (24) yields

$$v_i^* = \frac{(d_M - 1)^2}{2d_M} V_{\text{dc1}}. \tag{25}$$

Substituting (25) into (19) and (20) yields

$$\theta_2 = \pi \left(-\frac{d_M}{2} + 1 \right) \tag{26}$$

$$\theta_5 = \pi \left(\frac{d_M}{2} + 1 \right). \tag{27}$$

Similarly, substituting (25) into (21) and (22) yields

$$\theta_1 = \pi \frac{d_M}{2} \tag{28}$$

$$\theta_6 = \pi \left(-\frac{d_M}{2} + 2 \right). \tag{29}$$

From (12), (13), (26), (27), (28), and (29), the relationships $\theta_1 \le \theta_3$, $\theta_2 \le \theta_3$, $\theta_4 \le \theta_6$, and $\theta_5 \le \theta_6$ always hold in the range $0.5 \le d_M \le 1$.

Next, the validity of the assumptions that d_{A1} intersects tri_M at θ_2 and θ_5, while d_{A2} intersects tri_M at θ_1 and θ_6, respectively,

will be validated. Substituting (25) into (17) and (18) gives

$$d_{A1} = \begin{cases} -\frac{d_M}{2} + 1 & (0 \le \theta \le \theta_3, \theta_4 \le \theta \le 2\pi) \\ 0 & (\theta_3 < \theta < \theta_4) \end{cases} \tag{30}$$

$$d_{A2} = \begin{cases} \frac{d_M}{2} & (0 \le \theta \le \theta_3, \theta_4 \le \theta \le 2\pi) \\ 1 & (\theta_3 < \theta < \theta_4). \end{cases} \tag{31}$$

From Fig. 5, the values of $\mathrm{tri_M}$ at both θ_3 and θ_4 correspond to d_M. Meanwhile, the values of d_{A1} at θ_3 and θ_4 are obtained from (30) as $-d_M/2 + 1$, which always gives lower value than d_M in the range $0.67 \le d_M \le 1$. This signifies that the phase θ_2 that satisfies $\theta_2 \le \theta_3$, and the phase θ_5 that satisfies $\theta_5 \ge \theta_4$, consistently exist within the range. On the other hand, $-d_M/2 + 1$ gives higher value than d_M in the range $0.5 \le d_M < 0.67$. This signifies that the phases θ_2 and θ_5 do not exist within the range.

Meanwhile, the value of d_{A2} at θ_3 is obtained from (31) as $d_M/2$, which always gives lower value than d_M in the range $0.5 \le d_M \le 1$. This signifies that the phase θ_1 that satisfies $\theta_1 \le \theta_3$, and the phase θ_6 that satisfies $\theta_6 \ge \theta_4$, always exists in the given range. Subsequently, d_{A2} invariably intersects $\mathrm{tri_M}$ at θ_1 and θ_6.

The following analysis is done under $0.67 \le d_M \le 1$, while the analysis under $0.5 \le d_M < 0.67$ is provided in the Appendix. Based on KVL, (14), and (23), while including (4) in the calculation, the following relationship holds:

$$\begin{aligned} v_L &= v_M - v_A - V_{\mathrm{dc2}} \\ &= \begin{cases} V_{\mathrm{dc1}} - V_{\mathrm{dc2}} & (0 \le \theta \le \theta_1) \\ 0.5V_{\mathrm{dc1}} - V_{\mathrm{dc2}} & (\theta_1 < \theta \le \theta_2) \\ V_{\mathrm{dc1}} - V_{\mathrm{dc2}} & (\theta_2 < \theta \le \theta_3) \\ 0.5V_{\mathrm{dc1}} - V_{\mathrm{dc2}} & (\theta_3 < \theta \le \theta_4) \\ V_{\mathrm{dc1}} - V_{\mathrm{dc2}} & (\theta_4 < \theta \le \theta_5) \\ 0.5V_{\mathrm{dc1}} - V_{\mathrm{dc2}} & (\theta_5 < \theta \le \theta_6) \\ V_{\mathrm{dc1}} - V_{\mathrm{dc2}} & (\theta_6 < \theta \le 2\pi). \end{cases} \end{aligned} \tag{32}$$

Given that the relationship $d_M = V_{\mathrm{dc2}}/V_{\mathrm{dc1}} \ge 0.5$ holds, the inductor current rises with the rate of $V_{\mathrm{dc1}} - V_{\mathrm{dc2}}$ during $0 \le \theta \le \theta_1, \theta_2 < \theta \le \theta_3, \theta_4 < \theta \le \theta_5$, and $\theta_6 < \theta \le 2\pi$, and drops with the rate of $0.5V_{\mathrm{dc1}} - V_{\mathrm{dc2}}$ during $\theta_1 < \theta \le \theta_2, \theta_3 < \theta \le \theta_4$, and $\theta_5 < \theta \le \theta_6$. Further, the rising and dropping rates of the inductor current remain consistent under steady state. From Fig. 5, while considering (28), (29), and (32), the peak-to-peak ripple current in the range $0.67 \le d_M \le 1$ is obtained when the current steadily rises between $\theta_6 \le \theta \le 2\pi + \theta_1$

$$\begin{aligned} I_{\mathrm{ripple}} &= \frac{1}{\omega L} \int_{\theta_6}^{2\pi+\theta_1} (V_{\mathrm{dc1}} - V_{\mathrm{dc2}})\, d\theta \\ &= \frac{V_{\mathrm{dc1}}}{f_{SM} L} \frac{(1 - d_M) d_M}{2}. \end{aligned} \tag{33}$$

Similarly, it is possible to obtain I_{ripple} in the range $0 \le d_M < 0.5$, which is also separated into two range-divisions (i.e., $0 \le d_M < 0.33$ and $0.33 \le d_M < 0.5$). Finally, the values of I_{ripple} for all values of d_M are as follows.

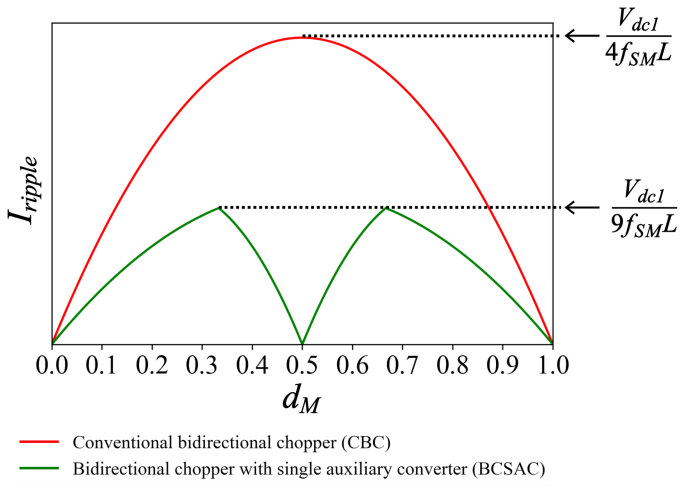

Fig. 6. Theoretical waveforms of switching-ripple current.

When $0 \le d_M < 0.33$

$$I_{\mathrm{ripple}} = \frac{V_{\mathrm{dc1}}}{f_{SM} L} \frac{(1 - d_M) d_M}{2}. \tag{34}$$

When $0.33 \le d_M < 0.5$

$$I_{\mathrm{ripple}} = \frac{V_{\mathrm{dc1}}}{f_{SM} L} (1 - 2d_M) d_M. \tag{35}$$

When $0.5 \le d_M < 0.67$

$$I_{\mathrm{ripple}} = \frac{V_{\mathrm{dc1}}}{f_{SM} L} (1 - d_M)(2d_M - 1). \tag{36}$$

When $0.67 \le d_M \le 1$

$$I_{\mathrm{ripple}} = \frac{V_{\mathrm{dc1}}}{f_{SM} L} \frac{(1 - d_M) d_M}{2}. \tag{37}$$

From (34) to (37), the maximum value of I_{ripple} can be obtained when $d_M = 1/3$ and $d_M = 2/3$

$$(I_{\mathrm{ripple}})_{\max} = \frac{V_{\mathrm{dc1}}}{9 f_{SM} L}. \tag{38}$$

On the other hand, $(I_{\mathrm{ripple}})_{\max}$ for the CBC is given by

$$(I_{\mathrm{ripple}})_{\max} = \frac{V_{\mathrm{dc1}}}{4 f_{SM} L}. \tag{39}$$

Thus, it is possible to reduce the ripple current by 4/9 using the single-cell auxiliary converter. Fig. 6 shows the theoretical waveforms of the ripple current, where the horizontal axis is d_M and the vertical axis is I_{ripple}. The red line shows the ripple current of the CBC, while the green line shows that of the BCSAC. Fig. 6 indicates that the advantage of BCSAC over the CBC is especially apparent when the converter operates in the vicinity of $d_M = 0.5$. Further, there is a symmetry between the BCSAC switching-ripple current when $d_M < 0.5$ and $d_M > 0.5$.

V. Comparison

It has been mentioned in Section I that the objective of the BCSAC is to achieve inductor volume reduction, compared to the application of CBC and TLFC, while considering the power

TABLE I
PARAMETERS OF THE THEORETICAL ANALYSES USED FOR THE COMPARISONS

Rated power	P	1.5 MW
DC-voltage source 1	V_{dc1}	1.5 kV
DC-voltage source 2	V_{dc2}	0.3−1.2 kV
Inductance (CBC)	L	0.9 mH
Inductance (TLFC)	L	0.45 mH
Inductance (BCAC)	L	0.015 mH
Inductance (BCSAC)	L	0.4 mH
DC-capacitor voltage (TLFC)	V_C	0.75 kV
DC-capacitor voltage (BCSAC)	V_C	0.75 kV
Switching frequency (main converter)	f_{SM}	5 kHz
Switching frequency (auxiliary converter)	f_{SA}	5 kHz
Switching frequency (TLFC)	f_{TLFC}	5 kHz

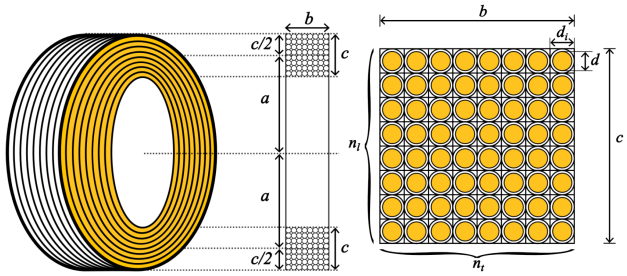

Fig. 7. Dimensions of (a) air-core inductor and (b) rectangular cross-section.

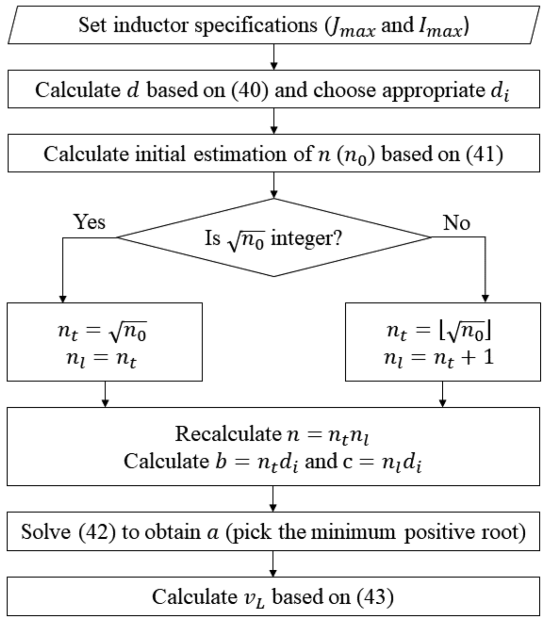

Fig. 8. Flowchart of the inductor volume analysis.

loss in the converter. To evaluate this, theoretical comparisons in respect to the inductor volume and power loss are conducted between CBC, TLFC [as shown in the Fig. 1(a)], BCAC [as shown in the Fig. 1(b)] with three cells, and BCSAC. However, cost comparison is beyond the scope of this article, and should be left for future work.

Table I summarizes the parameters used in the theoretical inductor-volume and power-loss analyses on all four choppers. The rated power is $P = 1.5$ MW. The high-voltage-side dc voltage is $V_{\text{dc1}} = 1.5$ kV, which is within the range of dc voltage supply commonly used in electric railway systems, while the low-voltage-side voltage is set between the range of $V_{\text{dc2}} = 0.3$ to 1.2 kV to conduct the analysis under different values of d_M [based on (11)]. The dc-capacitor voltage for both the TLFC and BCSAC are set to be half of V_{dc1} at $V_C = 0.75$ kV, while that of each cell in the BCAC is set to $V_C = 0.45$ kV. Finally, all choppers operate under the same switching frequency of 5 kHz (i.e., $f_{SM} = f_{SA} = f_{\text{TLFC}} = 5$ kHz). For the TLFC, the equivalent switching frequency could be $2f_{\text{TLFC}}$, depending on the relationship between V_{dc1} and V_{dc2}.

To do a fair comparison, the four choppers should produce the same amount of ripple current under the same switching frequency. Consequently, the inductance values are set to $L = 0.9, 0.45, 0.015$, and 0.4 mH for the CBC, TLFC, BCAC, and BCSAC, respectively. Air-core inductors are selected because they do not have core saturation, produce no iron loss, show better size reduction with increasing frequency, and are commonly used in railways [38], [39], [40]. Further, the inductors obey the Brooks coil geometry to give the highest possible inductance value for a given wire length [41]. Fig. 7 shows the air-core inductor and its rectangular cross-section dimensions. In the inductor, a denotes the distance between the axis of the winding and the axis of the inductor, while b and c denote the width and height of the winding cross-section, respectively. n_l denotes the number of layers, n_t denotes the number of turns per layer, n denotes the number of turns, d denotes the diameter of the wire without the insulation coating, and d_i denotes the diameter of the wire including the insulation coating.

The calculation method for these parameters have been given in Barrera-Cardenas et al.'s [41] work, where Fig. 8 shows the simplified flowchart of the calculation process. First, practical assumptions on the maximum current density, $J_{\max}$, and the maximum current, $I_{\max}$, are established. These assumptions should not be exceeded to avoid overheating. In the calculation, $J_{\max}$ is set to 2×10^6 A/m^2, while $I_{\max}$ is set to 1000 A. Then, d_i should be chosen based on the value of d that is obtained from

$$d = \sqrt{\frac{4I_{\max}}{\pi J_{\max}}}. \tag{40}$$

Further, the initial estimation of n (i.e., n_0) can be obtained by

$$n_0 = \sqrt[5]{\left(\frac{L}{2.029\mu_0 d_i}\right)^2}. \tag{41}$$

The values of n_t and n_l are obtained based on whether $\sqrt{n_0}$ is an integer or not, which will subsequently result in b and c, respectively (i.e., $b = n_t d_i$ and $c = n_l d_i$). Meanwhile, a can be obtained from the minimum positive root solution of

$$L = \frac{\mu_0 n^2 \pi a^3}{ab + 0.9a^2 + 0.32bc + 0.84ac} \tag{42}$$

TABLE II
PARAMETERS OF THE AIR-CORE INDUCTORS

Parameter	CBC	TLFC	BCAC	BCSAC
L	0.9 mH	0.45 mH	0.015 mH	0.4 mH
a	27.6 cm	25.6 cm	17.2 cm	23.8 cm
b	15.6 cm	13 cm	5.2 cm	13 cm
c	18.2 cm	15.6 cm	7.8 cm	15.6 cm
d	25.23 mm	25.23 mm	25.23 mm	25.23 mm
d_i	26 mm	26 mm	26 mm	26 mm
n_t	6	5	2	5
n_l	7	6	3	6
n	42	30	6	30
v_L	66.09 dm^3	45.50 dm^3	7.26 dm^3	40.73 dm^3

where μ_0 is the vacuum permeability ($\mu_0 = 1.257 \times 10^{-6}$). Finally, the inductor volume, v_L is given as

$$v_L = \pi b \left(a + \frac{c}{2}\right)^2. \tag{43}$$

The calculated parameters of the designed air-core inductors for all four choppers are shown in Table II. Under the same frequency, the BCSAC can reduce the inductor volume by 38.4% compared to the CBC, and by 10.5% compared to the TLFC. However, the volume-reduction achieved by the BCSAC is still lower than that achieved by the BCAC.

The IGBT power module 1MBI1000UG-330 from Fuji Electric (Si-IGBT, one-in-one, 3.3 kV) is chosen for all four choppers, where two modules are used in each of the CBC, the TLFC, and the main converter of the BCAC and BCSAC. The specifications of the 1MBI1000UG-330 module are given in [42]. Further, the IGBT power module CM1000DX-24 T is chosen for the TLFC, BCAC, and BCSAC, where two modules are used in the TLFC, 12 modules are used in the three-cells auxiliary converter of the BCAC, and four modules are used for the full-bridge auxiliary converter of the BCSAC. The specifications of the CM1000DX-24 T can be found in [43].

In the power loss analysis, the following losses are considered for all choppers.

1) IGBT conduction and switching losses.
2) Diode conduction and reverse recovery losses.
3) Inductor loss.

The formula to calculate these losses are commonly known in literature, such as [44], [45], and [46], while the values are approximated based on the data obtained from the datasheets. The IGBT conduction and switching losses can be determined by

$$P_{\text{IGBT-cond}} = \int^{T_{\text{IGBT-ON}}} \left(v_{\text{CE-sat}} i_L + R_{\text{lead}} {i_L}^2\right) dt \tag{44}$$

$$P_{\text{IGBT-sw}} = \frac{f_{\text{SW}}}{2} \int^{T_f + T_r} v_{\text{IGBT}} i_L \, dt. \tag{45}$$

The diode conduction and reverse recovery can be determined by

$$P_{\text{Diode-cond}} = \int^{T_{\text{Diode-ON}}} \left(v_f i_L + R_{\text{lead}} {i_L}^2\right) dt \tag{46}$$

$$P_{\text{Diode-rr}} = \frac{f_{\text{SW}}}{2} \int^{T_{rr}} v_{\text{Diode}} i_{\text{rr}} \, dt \tag{47}$$

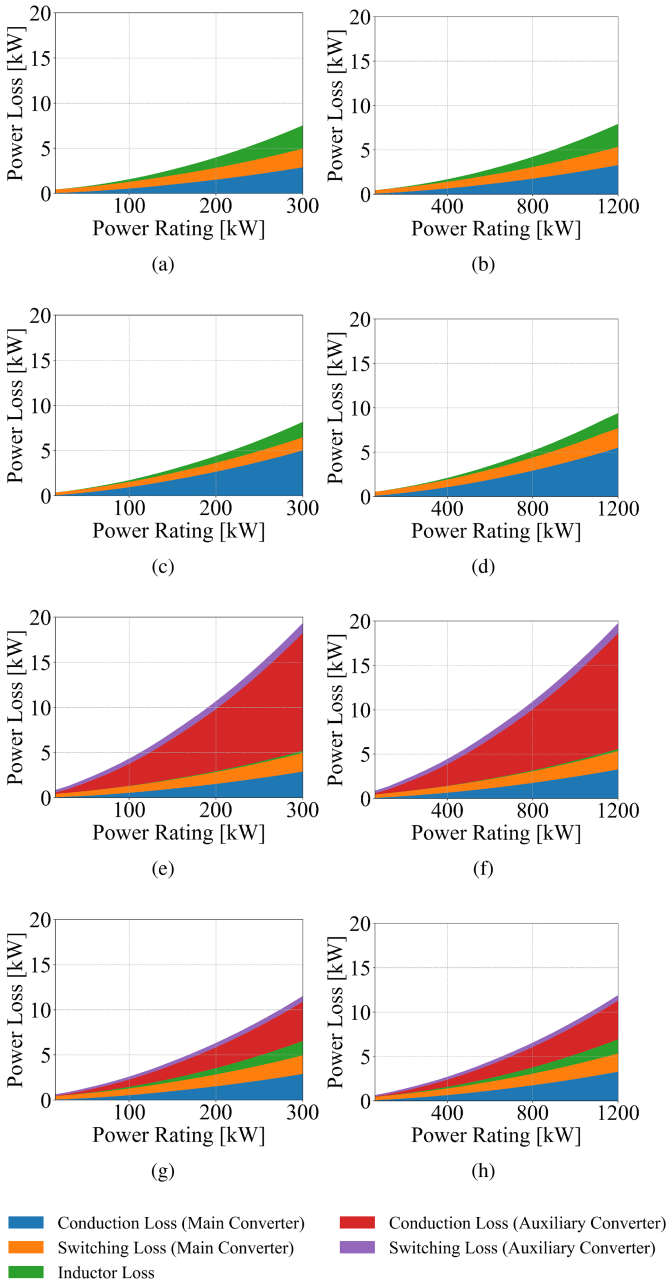

Fig. 9. Loss breakdown of (a) CBC when $V_{\text{dc2}} = 0.3$ kV, (b) CBC when $V_{\text{dc2}} = 1.2$ kV, (c) TLFC when $V_{\text{dc2}} = 0.3$ kV, (d) TLFC when $V_{\text{dc2}} = 1.2$ kV, (e) BCAC when $V_{\text{dc2}} = 0.3$ kV, (f) BSAC when $V_{\text{dc2}} = 1.2$ kV, (g) BCSAC when $V_{\text{dc2}} = 0.3$ kV, and (h) BCSAC when $V_{\text{dc2}} = 1.2$ kV.

where $v_{\text{CE-sat}}$ is the collector–emitter saturation voltage of the IGBT, v_f is the forward voltage of the diode, v_{IGBT} is the IGBT voltage, v_{Diode} is the diode voltage, i_{rr} is the reverse recovery current of the diode, and R_{lead} is the internal lead resistance of the IGBT. $T_{\text{IGBT-ON}}$, T_f, and T_r are the ON period, fall time, and rise time of the IGBT, respectively, while $T_{\text{Diode-ON}}$ and T_{rr} are the ON period and reverse-recovery time of the diode, respectively.

Fig. 9 shows the power losses breakdown of the four choppers under two different duty ratios (i.e., $d_M = 0.2$ and $d_M = 0.8$). The CBC loses around 7.8 kW in average under the maximum

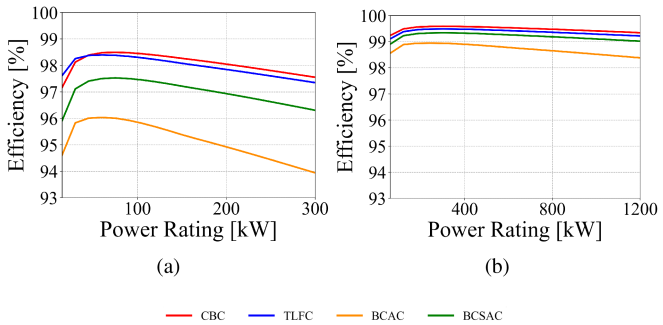

Fig. 10. Efficiency of the three choppers when (a) $V_{\mathrm{dc2}} = 0.3$ kV ($d_M = 0.2$) and (b) $V_{\mathrm{dc2}} = 1.2$ kV ($d_M = 0.8$).

TABLE III
COMPARISON RESULTS BETWEEN THE FOUR CHOPPERS

Comparison	CBC	TLFC	BCAC	BCSAC
Inductor volume	66.09 dm^3	45.50 dm^3	7.26 dm^3	40.73 dm^3
Power loss	7.7 kW	8.8 kW	19.5 kW	11.7 kW
Efficiency	97.2%–99.6%	97.4%–99.5%	94%–99%	96%–99.3%

power rating for both d_M values, where it is spread almost evenly among the conduction loss (3.1 kW), switching loss (2.1 kW), and inductor loss (2.6 kW). The TLFC total loss is slightly higher at 8.8 kW, where the conduction loss produces the majority at 5.3 kW, followed by the switching loss (1.8 kW) and the inductor loss (1.7 kW). Meanwhile, the BCAC produces a significantly higher loss (19.5 kW), where most of it comes from the added auxiliary converter with three cells (14.2 kW). Compared to the previous two topologies, the inductor loss is reduced to 0.2 kW. In comparison, the loss of the BCSAC is 11.7 kW, which is just slightly higher than those of the CBC and the TLFC, and significantly less than that of the BCAC. The reason is that the loss in the auxiliary converter is 5 kW, which is significantly less than that of the BCAC. Further, the inductor loss is 1.6 kW, which is still less than those produced by the CBC and TLFC.

The efficiency of the four choppers is then compared based on the power loss analysis results, as shown in Fig. 10, where red line indicates the CBC, blue line indicates the TLFC, orange line indicates the BCAC, and green line indicates the BCSAC. Under $d_M = 0.2$, the BCSAC is able to perform at around 97% in average, which is higher than the efficiency of BCAC at 95%, but lower than those of CBC and TLFC at 98%. Under $d_M = 0.2$, the BCSAC is able to perform at around 99.2% in average, which is higher than the efficiency of BCAC at 98.7%, but lower than those of CBC and TLFC at 99.5% and 99.4%, respectively.

Overall, there is a tradeoff between the inductor size and the power loss produced by the BCSAC, compared to the CBC, TLFC, and BCAC. Table III shows the summary of the comparison between the four choppers. However, considering the reduction in the inductor volume that can be achieved by the BCSAC, the slightly lower efficiency is a minor issue. In addition, reducing the volume of the inductor could reduce the energy required to move the vehicle, which could potentially positively impact the overall energy efficiency of the vehicle.

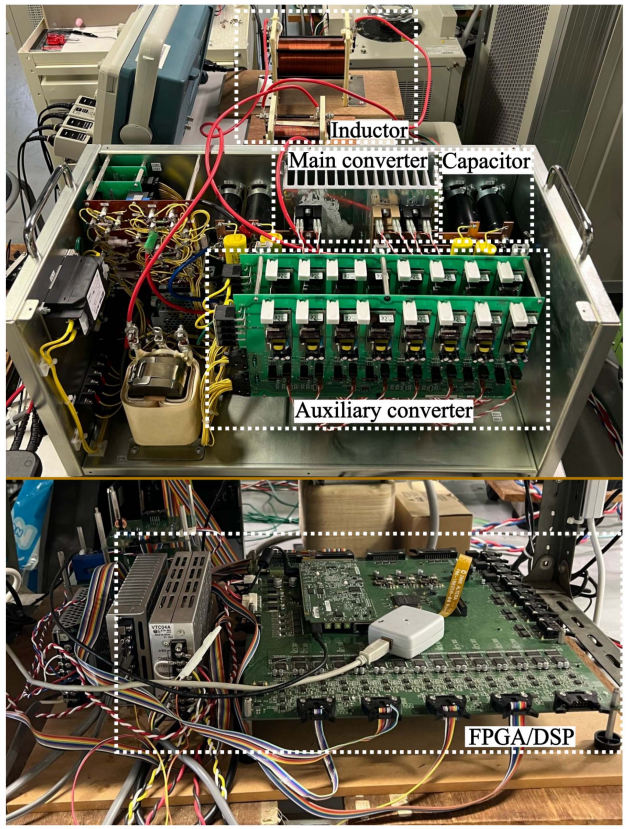

Fig. 11. Experimental setup using the downscaled model.

TABLE IV
PARAMETERS OF THE EXPERIMENTS

Rated power	P	2 kW
DC-voltage source 1	V_{dc1}	150 V
Inductance	L	0.395 mH
Capacitance	C	0.4 mF
DC-capacitor voltage	V_C^*	75 V
Switching frequency (main converter)	f_{SM}	5 kHz
Switching frequency (auxiliary converter)	f_{SA}	5 kHz

VI. EXPERIMENT

A. Experimental Conditions

Fig. 11 shows the downscaled model used in the experimental setup, while Table IV summarizes the experimental parameters. The model is set as the following.

1) The dc-voltage sources V_{dc1} and V_{dc2} are connected to either of dc-power supply KIKUSUI PAT160-50 T or HEADSPRING biATLAS-5D525.
2) The reference value for the dc-capacitor voltage is set to $V_C^* = 75$ V.
3) An air-core inductor with linear frequency characteristics and an inductance value of $L = 0.395$ mH is used, while the switching frequencies of the main and auxiliary converter are accordingly set to 5 kHz (i.e., $f_{SM} = f_{SA} = 5$ kHz).
4) The reference values for the inductor current can be alternately set to positive and negative values. Positive current

means that the power direction is from $V_{\rm dc1}$ to $V_{\rm dc2}$, while negative current means the opposite.

5) The controls of the BCSAC are achieved using a combination of Texas Instruments TMS320C6678 DSP and Altera Cyclone IV E EP4CE30F29C7 FPGA. The FPGA is used to generate the triangular carriers and to compare the duty ratios (i.e., d_M, d_{A1}, and d_{A2}) with the triangular carriers.
6) The experimental waveforms are taken using Tektronix oscilloscope DPO4104B-L with a frequency band of 1 GHz. i_L is measured using the Tektronix current probe TCP0020 with a frequency band of 50 MHz, while v_M, v_A, v_L, and v_C are measured using the Tektronix high-voltage differential probes THDP0200 with a frequency band of 200 MHz.

The following experiments are carried out to confirm the operations and controls of the BCSAC.

1) Ripple current values (including those of the CBC) when $V_{\rm dc1} = 150$ V, $i_L^* = \pm 10$ A, and v_C is initially charged to 75 V.
2) Steady-state operation when $V_{\rm dc1} = 150$ V, $V_{\rm dc2} = 65$ V, $i_L^* = 20$ A, and v_C is initially charged to 75 V.
3) Steady-state operation when $V_{\rm dc1} = 150$ V, $V_{\rm dc2} = 85$ V, $i_L^* = -20$ A, and v_C is initially charged to 75 V.
4) Transient behavior during initial charging of v_C from 0 to 30 V.
5) Transient behavior during step change of $V_{\rm dc2}$ from 65 to 75 V.

B. Switching-Ripple Current

Fig. 12 shows the results of the theoretical ripple current obtained from (34) to (37) and the experimental ripple current for both the CBC and the BCSAC based on the values of d_M under a) positive current, and b) negative current. The theoretical and experimental ripple currents of the CBC are illustrated by the red line and black crosses, respectively, while those of the BCSAC are illustrated by the green line and brown crosses, respectively. The experimental results shown in Fig. 12 are obtained under $V_{\rm dc1} = 150$ V, $V_{\rm dc2}$ is gradually changed from 30 to 140 V to alter the d_M, and $i_L^* = \pm 10$ A. Positive current implies that the current flows from the high-voltage side to the low-voltage side, while negative current implies that the current flows from the low-voltage side to the high-voltage side.

It can be seen from Fig. 12(a) and (b) that the experimental results agree well with the theoretical results for both choppers. The reason why there are small differences between the theoretical and experimental ripple currents for the BCSAC is the omission of v_B^* in the theoretical analysis. This affects the calculation of d_M, which consequently affect the calculation of $I_{\rm ripple}$. However, the differences are negligible if compared to the value of $I_{\rm ripple}$. Fig. 12(a) shows that the maximum experimental ripple current under $i_L^* = 10$ A for the CBC is 19 A (when $d_M = 0.47$), while that for the BCSAC is around 8.8 A (when $d_M = 0.32$ and 0.65). Fig. 12(b) shows that the maximum experimental ripple current under $i_L^* = -10$ A for the CBC is 19.2 A (when $d_M = 0.49$), while that for the BCSAC is around 8.7 A (when $d_M = 0.35$ and 0.68).

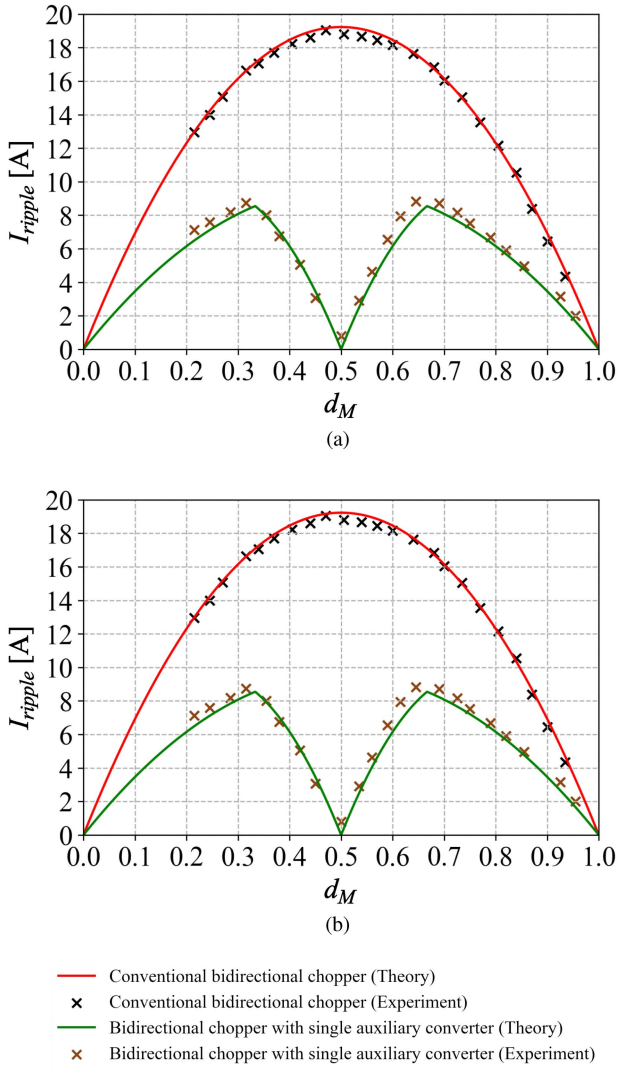

Fig. 12. Theoretical and experimental ripple currents of CBC and BCSAC under $V_{\rm dc1} = 150$ V, where (a) $i_L^* = 10$ A and (b) $i_L^* = -10$ A.

C. Steady-State Operation

Fig. 13 shows the steady-state experimental waveforms of the BCSAC when $V_{\rm dc1} = 150$ V, $V_{\rm dc2} = 65$ V, and $i_L^* = 20$ A. Positive current implies that the current flows from the high-voltage side to the low-voltage side. The main converter voltage, v_M, is a rectangular wave with dc and ac components, which alternates between $V_{\rm dc1}$ (= 150 V) and 0. Further, d_M is indicated to be 0.48, which is higher than the theoretical value of 0.43 obtained from (11), owing to the existence of v_B^* in the main converter control shown in Fig. 3. Meanwhile, the auxiliary converter voltage, v_A, alternates between $-V_C$ (= −75 V), 0, V_C (= 75 V).

As can be seen from Fig. 13, the dc-capacitor voltage, v_C, can be regulated at 75 V (= $V_{\rm dc1}/2$) with no steady-state error. Similarly, the inductor current, i_L, can be regulated at 20 A with no steady-state error. Further, the ripple current of i_L is shown to be 1.89 A, which agrees well with the maximum theoretical ripple current value of 1.46 A obtained from (35). The small difference in the experimental and theoretical values for the ripple current is caused by the v_B^* in the main converter control.

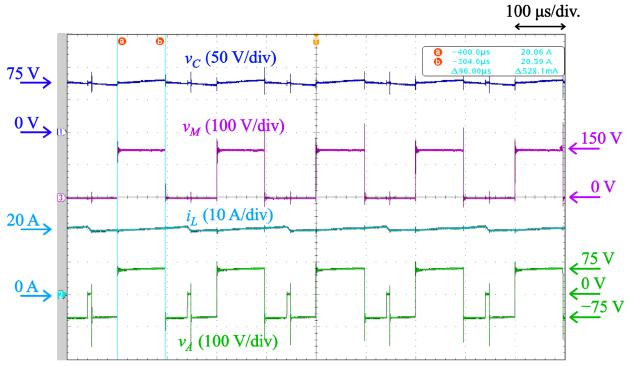

Fig. 13. Experimental steady-state waveform of BCSAC for $V_{\rm dc1} = 150$ V, $V_{\rm dc2} = 65$ V, and $i_L^* = 20$ A.

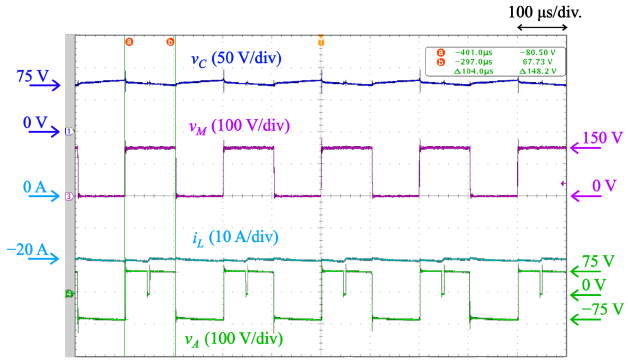

Fig. 14. Experimental steady-state waveform of BCSAC for $V_{\rm dc1} = 150$ V, $V_{\rm dc2} = 85$ V, and $i_L^* = -20$ A.

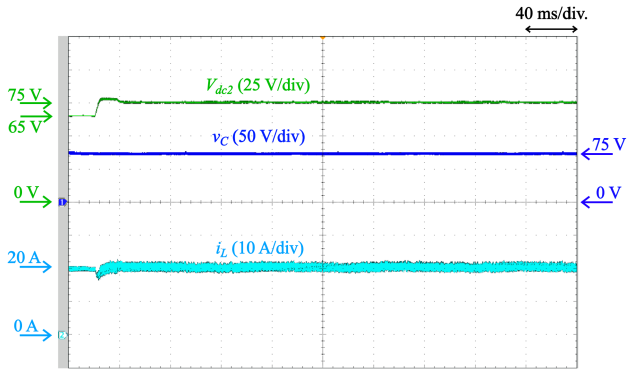

Fig. 15. Experimental waveform of BCSAC for $V_{\rm dc1} = 150$ V and $i_L^* = 20$ A, where there is a step change in $V_{\rm dc2}$ from 65 to 75 V.

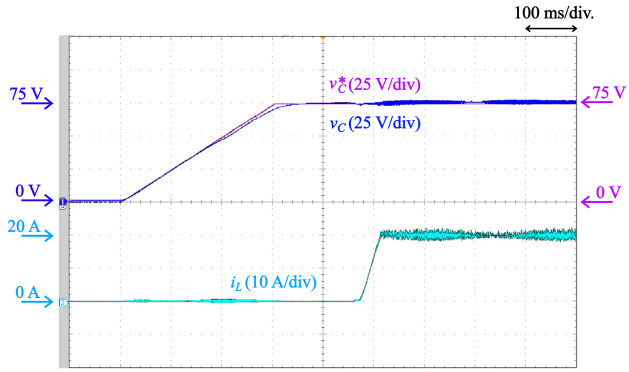

Fig. 16. Experimental waveform of BCSAC for $V_{\rm dc1} = 150$ V and $V_{\rm dc2} = 75$ V during the initial charging procedure.

Fig. 14 shows the steady-state experimental waveforms of the BCSAC when $V_{\rm dc1} = 150$ V, $V_{\rm dc2} = 85$ V, and $i_L^* = -20$ A. Negative current implies that the current flows from the low-voltage side to the high-voltage side. The main converter voltage, v_M, is a rectangular wave with dc and ac components, which alternates between $V_{\rm dc1}$ (= 150 V) and 0. Further, d_M is indicated to be 0.53, which is lower than the theoretical value of 0.57 obtained from (11), owing to the existence of v_B^* in the main converter control shown in Fig. 3. Meanwhile, the auxiliary converter voltage, v_A, alternates between $-V_C$ (= −75 V), 0, V_C (= 75 V).

As can be seen from Fig. 14, the dc-capacitor voltage, v_C, can be regulated at 75 V (= $V_{\rm dc1}/2$) with no steady-state error. Similarly, the inductor current, i_L, can be regulated at −20 A with no steady-state error. Further, the ripple current of i_L is shown to be 1.45 A, which agrees well with the maximum theoretical ripple current value of 2.14 A obtained from (36). The small difference in the experimental and theoretical values for the ripple current is caused by the v_B^* in the main converter control.

D. Transient-State Operation

Fig. 15 shows the transient experimental waveforms of the BCSAC when $V_{\rm dc1} = 150$ V and $i_L^* = 20$ A, while $V_{\rm dc2}$ is changed from 65 to 75 V under a step change. It is shown that $V_{\rm dc2}$ changes from 65 to 75 V in 20 ms with no overvoltage. There is a slight drop in the inductor current, i_L, at the initial part of the step change, which occurs due to the increasing $V_{\rm dc2}$ inversely affecting the inductor voltage, v_L. Further, the ripple current of i_L is increased when $V_{\rm dc2}$ is changed. This is because the change in $V_{\rm dc2}$ and d_M, added by the existence of v_B^*, will consequently affect the resulting ripple current. Meanwhile, the dc-capacitor voltage v_C can be stably regulated with no error even during the transient state.

Fig. 16 shows the transient experimental waveforms of the BCSAC when $V_{\rm dc1} = 150$ V and $V_{\rm dc2} = 75$ V during the initial charging procedure where the power is sent to the capacitor using $V_{\rm dc1}$. Initially, the full-bridge auxiliary converter is operated in charging mode, where S_3 and S_6 are ON, while S_4 and S_5 are OFF. In the main converter, S_2 is always OFF, while S_1 is controlled to charge the capacitor voltage, v_C. Specifically, the duty ratio of S_1, d_M, is determined using the traditional PI control to apply feedback control to v_C, where V_C^* is changed from zero to 75 V in 300 ms. After v_C reaches 75 V, the BCSAC operates normally, where i_L goes from zero to 20 A in approximately 40 ms. It can be seen from Fig. 16 that the initial charging procedure can be completed with neither overvoltage nor overcurrent occurring in the process.

VII. Conclusion

This article has presented a BCSAC with the following characteristics. 1) The switching frequencies of the main and auxiliary

converters are the same. 2) The dc-capacitor voltage is half of the dc-voltage-source voltage. Theoretical analysis done on the switching-ripple current shows that the proposed circuit can reduce the switching-ripple current under both positive and negative currents by 4/9, compared to the CBC. Consequently, based on the comparison made in this study, the BCSAC can achieve a 38.4% and 10.5% inductor volume reduction than that of the CBC and TLFC converter. The loss analysis has shown that the BCSAC produces slightly higher power loss than the CBC and TLFC, but significantly lower than that of the BCAC. Thus, high efficiency performance can still be achieved in the BCSAC operation. Finally, experimental results using a 2 kW downscaled model has verified the theoretical analysis on the switching-ripple current, as well as the operations and controls of the BCSAC in the steady states, under positive and negative currents, and transient states, during the initial charging procedure and under a step change.

APPENDIX

The following is the switching-ripple current analysis under $0.5 \leq d_M < 0.67$, where based on (30), the intersections between d_{A1} and tri_M do not exist. Consequently, v_A that was given by (23) is modified into:

$$v_A = \begin{cases} 0 & (0 \leq \theta \leq \theta_1) \\ V_C & (\theta_1 < \theta \leq \theta_3) \\ -V_C & (\theta_3 < \theta \leq \theta_4) \\ V_C & (\theta_4 < \theta \leq \theta_6) \\ 0 & (\theta_6 < \theta \leq 2\pi). \end{cases} \tag{48}$$

It should also be noted that the value of v_i^* here is different from the one given by (25), due to the nonexistence of θ_2 and θ_5. Substituting (12), (13), (21), (22), and (48) into (24) yields

$$v_i^* = \frac{(2d_M - 1)^2}{2d_M} V_{\text{dc1}}. \tag{49}$$

Substituting (49) into (21) and (22) yields

$$\theta_1 = \pi(2d_M - 1) \tag{50}$$

$$\theta_6 = \pi(3 - 2d_M). \tag{51}$$

From (12), (13), (50), and (51), the relationships $\theta_1 < \theta_3$ and $\theta_6 > \theta_4$ are always true within the range $0.5 \leq d_M < 0.67$.

Based on KVL, (14), and (48), while including (4) in the calculation, the following relationship holds:

$$\begin{aligned} v_L &= v_M - v_A - V_{\text{dc2}} \\ &= \begin{cases} V_{\text{dc1}} - V_{\text{dc2}} & (0 \leq \theta \leq \theta_1) \\ 0.5V_{\text{dc1}} - V_{\text{dc2}} & (\theta_1 < \theta \leq \theta_3) \\ 0.5V_{\text{dc1}} - V_{\text{dc2}} & (\theta_3 < \theta \leq \theta_4) \\ 0.5V_{\text{dc1}} - V_{\text{dc2}} & (\theta_4 < \theta \leq \theta_6) \\ V_{\text{dc1}} - V_{\text{dc2}} & (\theta_6 < \theta \leq 2\pi). \end{cases} \end{aligned} \tag{52}$$

Based on (52), the inductor current rises with the rate of $V_{\text{dc1}} - V_{\text{dc2}}$ during $0 \leq \theta \leq \theta_1$ and $\theta_6 < \theta \leq 2\pi$, and drops with the rate of $0.5V_{\text{dc1}} - V_{\text{dc2}}$ during $\theta_1 < \theta \leq \theta_6$. The rising and dropping rates remain consistent under steady state.

Since the current steadily drops from θ_1 until θ_6, the I_{ripple} under $0.5 \leq d_M < 0.67$ can be obtained by

$$\begin{aligned} I_{\text{ripple}} &= -\frac{1}{\omega L} \int_{\theta_1}^{\theta_6} (0.5V_{\text{dc1}} - V_{\text{dc2}})\, d\theta \\ &= \frac{V_{\text{dc1}}}{f_{SM} L}(1 - d_M)(2d_M - 1). \end{aligned} \tag{53}$$

Further, the values of d_{A1} and d_{A2} obtained by substituting (49) into (17) and (18) are the same with (30) and (31), respectively.

REFERENCES

[1] P. Arboleya, P. Bidaguren, and U. Armendariz, "Energy is on board: Energy storage and other alternatives in modern light railways," *IEEE Electrific. Mag.*, vol. 4, no. 3, pp. 30–41, Sep. 2016.

[2] V. I. Herrera, H. Gaztañaga, A. Milo, A. Saez-de Ibarra, I. Etxeberria-Otadui, and T. Nieva, "Optimal energy management and sizing of a battery–supercapacitor-based light rail vehicle with a multiobjective approach," *IEEE Trans. Ind. Appl.*, vol. 52, no. 4, pp. 3367–3377, Jul./Aug. 2016.

[3] X. Liu and K. Li, "Energy storage devices in electrified railway systems: A review," *Transp. Saf. Environ.*, vol. 2, no. 3, pp. 183–201, 2020. [Online]. Available: https://doi.org/10.1093/tse/tdaa016

[4] C. Wu, S. Lu, F. Xue, L. Jiang, and M. Chen, "Optimal sizing of onboard energy storage devices for electrified railway systems," *IEEE Trans. Transport. Electrific.*, vol. 6, no. 3, pp. 1301–1311, Sep. 2020.

[5] D. Ramsey, T. Letrouve, A. Bouscayrol, and P. Delarue, "Comparison of energy recovery solutions on a suburban dc railway system," *IEEE Trans. Transport. Electrific.*, vol. 7, no. 3, pp. 1849–1857, Sep. 2021.

[6] Z. Li, S. Hoshina, N. Satake, and M. Nogi, "Development of dc/dc converter for battery energy storage supporting railway dc feeder systems," *IEEE Trans. Ind. Appl.*, vol. 52, no. 5, pp. 4218–4224, Sep./Oct. 2016.

[7] S. P. Sunddararaj, S. S. Rangarajan, U. Subramaniam, E. R. Collins, and T. Senjyu, "A new topology of dc-dc converter with bidirectional power flow capability coupled with a nine multilevel inverter for EV applications," in *Proc. 7th Int. Conf. Elect. Energy Syst.*, 2021, pp. 177–182.

[8] M. S. Perdigão, J. P. Trovão, J. M. Alonso, P. G. Pereirinha, and E. S. Saraiva, "Experimental large-signal characterization of power inductors in bidirectional electric vehicle dc-dc converters for simulation analysis," in *Proc. 15th Eur. Conf. Power Electron. Appl.*, 2013, pp. 1–10.

[9] B. L. Lawu, S. Fuada, S. Ramadhan, A. F. Sabana, and A. Sasongko, "Charging supercapacitor mechanism based-on bidirectional dc-dc converter for electric ATV motor application," in *Proc. Int. Symp. Electron. Smart Devices*, 2017, pp. 129–132.

[10] K. Ogura et al., "Test results of a high capacity wayside energy storage system using Ni-MH batteries for dc electric railway at new york city transit," in *Proc. IEEE Green Technol. Conf.*, 2011, pp. 1–6.

[11] A. Verdicchio, P. Ladoux, H. Caron, and C. Courtois, "New medium-voltage dc railway electrification system," *IEEE Trans. Transport. Electrific.*, vol. 4, no. 2, pp. 591–604, Jun. 2018.

[12] N. Soltau, E. Wiesner, E. Stumpf, S. Idaka, and K. Hatori, "Electric-energy savings using 3.3 kv full-SiC power-modules in traction applications," in *Proc. 15th Int. Conf. Ecological Veh. Renewable Energies*, 2020, pp. 1–5.

[13] K. Yasui et al., "A 3.3 kv 1000 a high power density SiC power module with sintered copper die attach technology," in *Proc. PCIM Europe Int. Exhib. Conf. Power Electron., Intell. Motion, Renewable Energy Energy Manag.*, 2019, pp. 1–6.

[14] T. Shioi et al., "Battery management system with flying capacitor converter operated in discontinuous current mode," in *Proc. 20th Int. Symp. Power Electron.*, 2019, pp. 1–6.

[15] J.-i. Itoh, R. Ishibashi, H. N. Le, N. Takaoka, K. Kusaka, and K. Tanabe, "Control method of flying capacitor converter operated in discontinuous current mode and critical current mode," in *Proc. IEEE Energy Convers. Congr. Expo.*, 2018, pp. 155–161.

[16] Z. Chen et al., "A wide conversion ratio three-level dc-dc converter with loop-free self-balancing technique of flying capacitor," in *Proc. IEEE Int. Symp. Circuits Syst.*, 2023, pp. 1–5.

[17] J. Wei, B. Hu, and Y. Xian, "Research on three-level bi-directional dc-dc converter and its control strategy used for energy storage system of electric wheeled tramcar," in *Proc. IEEE 16th Conf. Ind. Electron. Appl.*, 2021, pp. 2048–2052.

[18] V. Jayan, A. Ghias, and A. Merabet, "Modeling and control of three-level bi-directional flying capacitor dc- dc converter in dc microgrid," in *Proc. 45th Annu. Conf. IEEE Ind. Electron. Soc.*, vol. 1, 2019, pp. 4113–4118.
[19] D. Zhang, C. Chen, Y. Ou, T. Zheng, and W. Tang, "Model predictive control of three-level bidirectional dc-dc converter based on super capacitor energy storage system," in *Proc. Int. Conf. Elect. Eng.*, 2020, pp. 1–5.
[20] S. Mersche, M. Bayer, K. Rickert, and M. Hiller, "Analysis of balancing algorithms for quasi- two/three-level single phase operation of a flying capacitor converter," in *Proc. 24th Eur. Conf. Power Electron. Appl.*, 2022, pp. 1–10.
[21] Z. Chen, S. Liu, Y. Chen, X. Fan, and Y. Ma, "A current-injection-based flying capacitor balancing circuit for three-level dc-dc converter," in *Proc. IEEE Int. Symp. Circuits Syst.*, 2022, pp. 2630–2634.
[22] D. H. Zhou, J. Celikovic, Y. Elasser, D. Maksimovic, and M. Chen, "Balancing limits of flying capacitor voltages in coupled inductor FCML converters," in *Proc. IEEE 23rd Workshop Control Model. Power Electron.*, 2022, pp. 1–8.
[23] N. B. Sagpazar, W. Cho, K. Kim, and S. Choi, "Three-level resonant switched capacitor boost converter," in *Proc. 10th Int. Conf. Power Electron. ECCE Asia*, 2019, pp. 2868–2873.
[24] A. Salehian, S. S. Hashemi, R. Beiranvand, and A. Yazdian, "Simulation of a step-up resonant switched-capacitor converter under the CCM operation mode," in *Proc. 10th Int. Power Electron., Drive Syst. Technol. Conf.*, 2019, pp. 230–235.
[25] M. Forouzesh, Y. P. Siwakoti, S. A. Gorji, F. Blaabjerg, and B. Lehman, "Step-up dc–dc converters: A comprehensive review of voltage-boosting techniques, topologies, and applications," *IEEE Trans. Power Electron.*, vol. 32, no. 12, pp. 9143–9178, Dec. 2017.
[26] W. Xie and K. Smedley, "General full-range regulation method for resonant switched-capacitor converters," in *Proc. IEEE Int. Power Electron. Application Conf. Expo.*, 2022, pp. 1025–1029.
[27] S. Goodarzi, R. Beiranvand, R. Rezaii, M. A. Abolhasani, and M. Mohamadian, "Design and implementing of a novel resonant switched-capacitor converter for improving balancing speed of lithium-ion battery cells," in *Proc. 7th Power Electron. Drive Syst. Technol. Conf.*, 2016, pp. 204–210.
[28] K. Sano and H. Fujita, "Performance of a high-efficiency switched-capacitor-based resonant converter with phase-shift control," *IEEE Trans. Power Electron.*, vol. 26, no. 2, pp. 344–354, Feb. 2011.
[29] A. Mousavi, P. Das, and G. Moschopoulos, "A comparative study of a new ZCS dc–dc full-bridge boost converter with a ZVS active-clamp converter," *IEEE Trans. Power Electron.*, vol. 27, no. 3, pp. 1347–1358, Mar. 2012.
[30] H. Ohnishi and M. Hagiwara, "Experimental verification of a bidirectional chopper for battery energy storage systems capable of reduction in size and weight of an inductor," in *Proc. IEEE Energy Convers. Congr. Expo.*, 2017, pp. 197–204.
[31] H. J. Ahmad, H. Ohnishi, and M. Hagiwara, "Start-up and transient operation of a bidirectional chopper with an auxiliary converter," in *Proc. Int. Power Electron. Conf.*, 2018, pp. 3273–3279.
[32] H. J. Ahmad and M. Hagiwara, "Interleaved bidirectional chopper with auxiliary converters for battery energy storage systems," in *Proc. IEEE Appl. Power Electron. Conf. Expo.*, 2020, pp. 2090–2097.
[33] H. J. Ahmad and M. Hagiwara, "Interleaved bidirectional chopper with auxiliary converters for dc electric railways," *IEEE Trans. Power Electron.*, vol. 36, no. 5, pp. 5336–5347, May 2021.
[34] M. Hagiwara and H. J. Ahmad, "High switching frequency operation of bidirectional chopper with auxiliary converter for dc electric railways," in *Proc. IEEE Int. Future Energy Electron. Conf.*, 2021, pp. 1–6.
[35] H. J. Ahmad and M. Hagiwara, "A compact high-power noninverting bidirectional buck–boost chopper for onboard battery energy storage systems," *IEEE Trans. Power Electron.*, vol. 37, no. 2, pp. 1722–1735, Feb. 2022.
[36] N. Hassanpour, A. Chub, A. Blinov, and D. Vinnikov, "Comparison of full power and partial power buck-boost dc-dc converters for residential battery energy storage applications," in *Proc. IEEE 16th Int. Conf. Compatibility, Power Electronics, Power Eng.*, 2022, pp. 1–6.
[37] G. A. M. Nasution, M. Matsumoto, and M. Hagiwara, "Switching-ripple current evaluation of bidirectional chopper with single auxiliary full-bridge converter," in *Proc. IEEE Energy Convers. Congr. Expo.*, 2023, pp. 6357–6364.
[38] C. Rindfleisch and B. Wicht, "Efficiency impact of air-cored inductors in multi-MHz power converters," in *Proc. 18th Eur. Conf. Power Electron. Appl.*, 2016, pp. 1–8.
[39] R. T. Naayagi and A. J. Forsyth, "Design of high frequency air-core inductor for dab converter," in *Proc. IEEE Int. Conf. Power Electron., Drives Energy Syst.*, 2012, pp. 1–4.
[40] G. Abad, *Power Electronics and Electric Drives for Traction Applications*. Hoboken, NJ, USA: Wiley, Incorporated, 2016. [Online]. Available: https://books.google.co.jp/books?id=_loanQAACAAJ
[41] R. Barrera-Cardenas, T. Isobe, and M. Molinas, "Optimal design of air-core inductor for medium/high power dc-dc converters," in *Proc. IEEE 17th Workshop Control Model. Power Electron.*, 2016, pp. 1–8.
[42] 2013. [Online]. Available: https://felib.fujielectric.co.jp/en/M10013/M20088/document_detail/b9ca89b2-8198-4480-9ebd-b8f5dd0a17ed
[43] 2020. [Online]. Available: https://www.mitsubishielectric.com/cn/semiconductors/powerdevices/datasheets/igbt/t_series/cm1000dx-24t_e.pdf
[44] J. Qi et al., "Temperature dependence of dynamic performance characterization of 1.2-kv SiC power MOSFETs compared with Si IGBTs for wide temperature applications," *IEEE Trans. Power Electron.*, vol. 34, no. 9, pp. 9105–9117, Sep. 2019.
[45] T. Zhao, J. Wang, A. Q. Huang, and A. Agarwal, "Comparisons of SiC MOSFET and Si IGBT based motor drive systems," in *Proc. IEEE Ind. Appl. Annu. Meeting*, 2007, pp. 331–335.
[46] M. Alam, K. Kumar, and V. Dutta, "Comparative efficiency analysis for silicon, silicon carbide MOSFETs and IGBT device for dc–dc boost converter," *SN Appl. Sci.*, vol. 1, no. 1700, p. 5, 2019.

Ghiffari Aby Malik Nasution (Student Member, IEEE) was born in Bekasi, Indonesia, in 1997. He received the B.Eng. degree in transdisciplinary science and engineering and the M.Eng. degree in energy science and engineering from the Tokyo Institute of Technology, Tokyo, Japan, in 2020 and 2022, respectively. He is currently working toward the Ph.D. degree in energy science and engineering with the Department of Electrical and Electronic Engineering, Tokyo Institute of Technology.

His research interests include dc–dc converters for hybrid renewable energy system and electric trains/vehicles.

Masaki Matsumoto was born in Ibaraki, Japan, in 1999. He received the B.S. degree in electrical and electronic systems engineering from Ibaraki University, Ibaraki, Japan, in 2022, and the M.S. degree in electrical and electronic engineering from the Tokyo Institute of Technology, Tokyo, Japan, in 2024, respectively.

Since 2024, he has been with Sony Corporation, Tokyo, Japan.

Makoto Hagiwara (Senior Member, IEEE) was born in Tokyo, Japan, in 1979. He received the B.S., M.S., and Ph.D. degrees in electrical engineering from the Tokyo Institute of Technology, Tokyo, Japan, in 2001, 2003, and 2006, respectively.

From 2006 to 2015, he was an Assistant Professor with the Department of Electrical and Electronic Engineering, Tokyo Institute of Technology. Since 2015, he has been an Associate Professor with the Tokyo Institute of Technology. His research interests include dc-to-dc converters for electric trains/vehicles, high-voltage high-power converters for utility applications and renewable energies, and HVDC technologies.

Dr. Hagiwara was a recipient of the 2010 International Power Electronics Conference (IPEC-Sapporo/ECCE-Asia) second prize paper award, the 2012 and 2013 IEEE Industry Applications Society Industrial Power Converter Committee first prize paper awards, the 2014 Isao Takahashi Power Electronics Award, the 2023 TPEL AE Excellence Award, and the 2024 Nagamori Award. The total citation index for all his papers in Google Scholar is more than 7000.